small methods
www.small-methods.com

Self-Powered Cursor Using a Triboelectric Mechanism

*Han Wu, Qiongfeng Shi, Fei Wang, Aaron Voon-Yew Thean, and Chengkuo Lee**

This work reports the complete theoretical modeling, simulation, and experimental characterization of a self-powered cursor based on triboelectric nanogenerator (TENG). The self-powered cursor is made of liquid-metal and polydimethylsiloxane (PDMS) mixture that deforms and contacts with different sensing electrodes under different applied force. The self-powered cursor has the capability of simultaneously detecting normal force (0–25 N) and shear force direction (0°–360°) for the first time. The normal force sensing is characterized by open-circuit voltage, charge, and current with the sensitivity of 0.131 V N^{-1}, 0.048 nC N^{-1}, and 0.175 nA N^{-1}, respectively. The shear force direction detection can achieve a direction resolution of 15°. Because of the high output voltage and low internal impedance, the self-powered cursor is readily compatible with commercial portable circuits without the requirement of specified bulky high-impedance instruments to detect the output voltage. Demonstration of the self-powered cursor as a triggering signal to drive a small vehicle is successfully realized by directly detecting the output voltage without any periphery signal processing circuits. The robust structure, stable output performance, and self-powered sensing property enable the self-powered cursor as an ideal human machine interface towards batteryless, energy saving, and environmentally friendly applications.

1. Introduction

Tactile sensor or touch sensor has stimulated huge research interest in recent years.[1,2] These sensors are embedded into conceptual Internet of Things (IoT) applications such as medical devices, industrial controls, health and safety devices, augment reality interaction between human and computers, supply chain tools, etc. According to the prediction by Cisco,[3] there will be trillions of sensors distributed around the earth by 2020. It is reasonable to expect that the tactile sensors will share quite a huge proportion in the trillions of sensors. As current sensors are powered by batteries with limited lifetime, such huge quantity of exhausted batteries distributed around the world will cause serious environmental issues. Therefore, self-powered sensors have been developed rapidly as a solution. Specifically, self-powered tactile sensors attract increasing attentions due to its self-generated working mechanism and energy saving capability for IoT applications.

By transforming mechanical energy to electrical energy, self-powered touch sensors can generate voltage, current, or charge to indicate the property of applied force, i.e., normal force component and shear force component. With the merits of wide material range, simple fabrication process, cost-effectiveness, and large output performance, self-powered pressure sensors based on triboelectric nanogenerator (TENG) have attracted extensive research efforts recently.[4–15] It is a promising technology for solving the issues in economic development, energy saving, and environment protection. Many high-performance tactile or pressure sensors based on TENG have been prototyped and investigated. For example, Wang and co-workers have reported a tactile sensor with high sensitivity of 44 mV Pa^{-1} in low pressure range (<0.15 kPa).[9] Shi et al. proposed a liquid triboelectric-based microfluidic sensor for pressure sensing and finger motion monitoring.[14] Meng et al. developed a micropatterned polydimethylsiloxane (PDMS) touch sensor with high output performance.[15] However, general forces

H. Wu, Q. Shi, Prof. A. V.-Y. Thean, Prof. C. Lee
Department of Electrical & Computer Engineering
National University of Singapore
4 Engineering Drive 3, Singapore 117576, Singapore
E-mail: elelc@nus.edu.sg

H. Wu, Prof. F. Wang
Department of Electrical and Electronic Engineering
Southern University of Science and Technology
Xueyuan Road 1088, Nanshan District, Shenzhen,
Guangdong 518055, China

The ORCID identification number(s) for the author(s) of this article can be found under https://doi.org/10.1002/smtd.201800078.

DOI: 10.1002/smtd.201800078

Q. Shi, Prof. C. Lee
Center for Sensors and MEMS
National University of Singapore
4 Engineering Drive 3, Singapore 117576, Singapore

Q. Shi, Prof. C. Lee
National University of Singapore Suzhou Research Institute (NUSRI)
Suzhou Industrial Park, Suzhou 215123, China

Q. Shi, Prof. A. V.-Y. Thean, Prof. C. Lee
Hybrid-Integrated Flexible (Stretchable) Electronic Systems Program
National University of Singapore
5 Engineering Drive 1, Singapore 117608, Singapore

Prof. C. Lee
NUS Graduate School for Integrative Science and Engineering
National University of Singapore
Singapore 117456, Singapore

are composed of normal and shear components. Although the normal force components were characterized by touch sensors with high sensitivity and robust performance based on TENG in recent researches,[13,16–19] the shear force components with direction information are rarely studied by TENG–based sensors.

Previously, many of TENG models are explained by circuit modes.[4,20–22] Under the circuit explanations, the TENGs are more likely working in vertical contact-separation mode or in-plane sliding mode.[2] Working under these two modes, large displacement needs to be applied between layers of TENGs to achieve high output. It results in the consequence that TENGs need to occupy large space which makes it difficult for shrink-down applications. More recently, Dharmasena et al. built up a distance-dependent electric field model for TENG based on Maxwell equations.[23] Wang also proposed explanations for triboelectric and piezoelectric nanogenerators based on Maxwell displacement current.[24] The electric field and displacement current theories can be adopted as guidance for designing TENG sensors that are not working in these two modes with robustness, stable output, and small structure deformations.[2]

This work will focus on analyzing the working mechanism of self-powered cursor according to the electric field theory and characterization of the device for normal force and shear force detection. The self-powered cursor has the capability of detecting not only the normal force but also the shear force directions. For normal force sensing, it has a linear range of 0–25 N. The open-circuit voltage, output charge, and short-circuit current sensitivity are 0.131 V N^{-1}, 0.048 nC N^{-1}, and 0.175 nA N^{-1}, respectively. Because the theoretical model is limited in 1D or 2D in previous works,[13,16–19] the shear force part is not able to be revealed by TENG. Here, from the electric field perspective, the 3D force information is able to be characterized by the electric field variations due to force applied on the device. Besides, the flexibility of liquid metal and 3D printing structure ensure that the device has a robust force detecting capability. In the aspect of shear force detection, it can resolve the shear force direction with step resolution of at least 15°. Additionally, this self-powered cursor is also able to detect the rotation motions applied on the touch point. This self-powered cursor shows significant potential in the batteryless and energy saving IoT sensor applications.

2. Working Mechanism Model

Based on the electrical field theory of TENG, the working mechanism of the self-powered cursor under normal force is explained in **Figure 1**a. As shown in the sketch, the self-powered cursor consists of top semisphere touch point, bottom functional semisphere, polytetrafluoroethylene (PTFE) thin film, aluminum electrode, and supporting structure. The bottom semisphere is made by mixing galinstan (eutectic alloy of 68.5% gallium, 21.5% indium, and 10% tin by weight) with PDMS. The galinstan–PDMS mixture functions as one triboelectric layer and conductive material during the pressing period as Fassler and Majidi uncovered.[25] The surface topography of galinstan–PDMS mixture is shown in Figure S1a–c (Supporting Information).

Because of the work function difference between galinstan and PTFE,[26,27] negative charges will transfer from galinstan surface to PTFE when they contact with each other. Then, galinstan holds net positive charge and PTFE surface carries net negative charge. Due to Coulomb's law, the total charge induced in the aluminum electrode is contributed by the negative charge on PTFE surface and the positive charge on galinstan surface. However, the negative charge on PTFE surface almost has no change after several periods of fully contacting. When no force is applied, positive charge is widely separated in the semisphere of galinstan–PDMS mixture to maintain the electrostatic equilibrium. After force is applied, the positive charge on mixture is attracted significantly by the negative charge on PTFE in the contacting area. The charge density of the galinstan surface in the contacting area changes dramatically. The electric field generated by the positive charge is also enhanced under the contacting area. Corresponding charge pair would be induced in the aluminum electrode. The charge pair is approximately the same amount of positive charge accumulated in the contacting area of galinstan. After force is released and the deformed structure recovers to initial shape, the electric field is weakened and the charge pairs are also reduced. When the electrode is connected to ground with a resistor in Figure 1b, the induced positive charge in the electrode would flow to the ground to keep electrostatic equilibrium. This is the basic qualitative working mechanism of the self-powered cursor under normal force.

Based on Gauss's law, the electric field at fixed positions is proportional to the source charge amount Q. Therefore, Q is calculated by combination of Equations (S1)–(S4) (Supporting Information) to characterize the property of electric field acting on the bottom aluminum electrode. The charges aggregated on galinstan of contacting area are derived as

$$Q = \pi e D_\mathrm{s}(W_\mathrm{m} - W_\mathrm{p}) \cdot \left[\frac{3F\left(\dfrac{1-\upsilon_1^2}{E_1} + \dfrac{1-\upsilon_2^2}{E_2} \right)}{4\dfrac{1}{R}} \right]^{\frac{2}{3}} \tag{1}$$

where e is the charge of an electron, D_s is the number of surface states per unit area and unit energy, W_m and W_p are the work functions for the metal gallium and PTFE, E_1 and E_2 are the modulus of elasticity for galinstan–PDMS mixture and PTFE film, υ_1 and υ_2 are the Poisson's ratios, respectively, F is the applied force on the top dome, and R is the radius of sphere. Here, gallium's work function has been used to represent the work function of galinstan, for that gallium has consisted the main part of the eutectic alloy as the energy-dispersive X-ray spectroscopy image shown in Figure S1d (Supporting Information). The specific values of parameters are available in Table S1 (Supporting Information).

As the maximum distance change between vertex and nadir of sphere is 10 mm which is the diameter, the theoretical

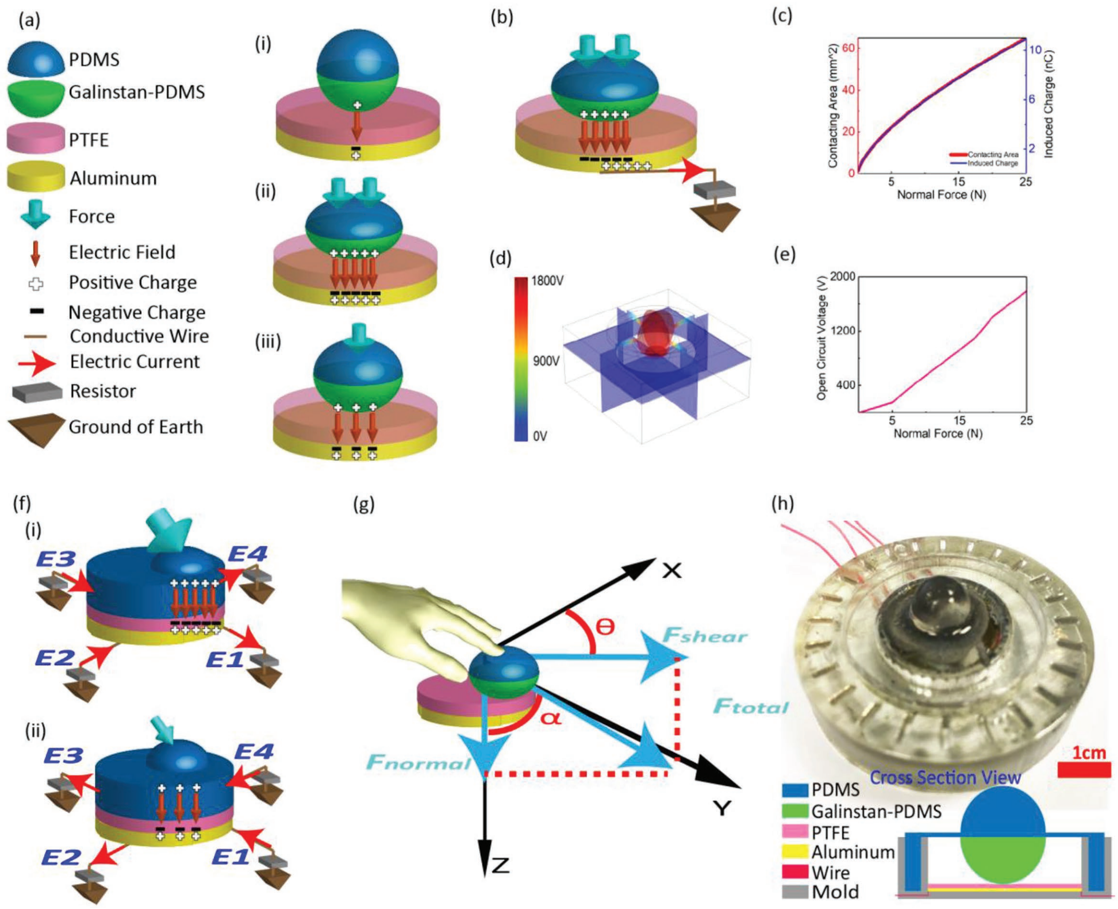

Figure 1. a) Working mechanism of the self-powered cursor under normal force based on the electric field change with the applied force. b) Net induced charge. c) The relationship of contacting area and induced charge with the applied force. d) Multislice electrical potential distribution. e) The relationship of open-circuit voltage with the applied force. f) The structure with multiple electrodes and working mechanism for shear force detection. g) Force component analysis acting on self-powered cursor. h) Photo of self-powered cursor and its cross-section view.

maximum applied force is calculated as 25 N. Relationships of the contact area A, induced charge Q, and applied force F is shown in Figure 1c, in which the contact area curve and induced charge curve are overlapping with each other. The relationship of contacting area with applied force is almost linear in the range of 0–25 N. Meanwhile, the induced charge Q also has a linear relationship with applied force in the range of 0–25 N.

In sensor applications, voltage has huge significance in characterizing the sensor performance for its convenience to be read by circuits. A self-powered cursor is better to have voltage output around 0–5 V which can be directly read by commercial portable circuits without any periphery processing circuit. Therefore, the voltage output of the bottom aluminum electrode relative to the earth ground should be derived to characterize the intended sensor performance. In the metal and insulator contacting model, the charge distribution in metal is mathematically difficult to be calculated. That means that the electric field and electric potential are not able to be resolved through manual calculation. However, finite element modeling offers an effective method to simulate the voltage potential of the bottom electrode when the sphere deforms. A finite element simulation is built up to solidify the qualitative analysis and quantitative derivations. The multislice electrical potential distribution and open-circuit voltage of bottom aluminum electrode are shown in Figure 1d,e, respectively. It can be observed that the open-circuit voltage has an approximately linear relationship with the applied force which is in accordance with the theoretical derivations. Although the maximum output voltage is around 1800 V which is quite high, this simulation is built up in the vacuum circumstance. Additionally, recent research of TENG in vacuum environment also solidified that the output voltage level is reasonable.[28]

In the above descriptions, the force is the normal force. In natural environments, forces are more likely to be random containing both the normal force component and the shear force component. The normal force is measured through the above mentioned mechanism. The shear force can be simultaneously measured by the same mechanism with multiple electrodes. The device with multiple electrodes and working mechanism is shown in Figure 1f. There are in total four electrodes under the PTFE sheet to perceive the charge distribution changes on galinstan surface as the applied force changes. The PDMS film, circling around the sphere, confines the sphere position in the center. To demonstrate the working mechanism, the shear force is applied toward electrode 1 (E1) and electrode 4 (E4), as shown in Figure 1f(i). The electric field on E1 and E4 generated by galinstan in the contacting area is enhanced comparing with the initial electric field. On the contrary, the electric field on electrode 2 (E2) and electrode 3 (E3) generated by galinstan in the contacting area is weakened comparing with the initial state. Therefore, the current flows from E1 and E4 to the ground and flows from the ground to E2 and E3. When the force is released, as shown in Figure 1f(ii), the electric fields are back to the initial state and current flows in the opposite direction. Since charge output, open-circuit voltage, and short-circuit current of each electrode have proportional relationship with force components shared on the corresponding electrodes, force magnitude and direction can be determined by outputs of different electrodes.

Although force consisted of the normal force component and the shear force component, as shown in Figure 1g, the shear force component dominates the total force in the applications of touching a cursor to realize controlling different direction, namely, the vertical angle α, between total force and normal force, is greater than 60°. When force is acting on its top dome, finally the shear force resolved into the compressing and elongation of PDMS film which circles around the sphere and confines the sphere positions. The normal force component contributes to form the contacting area which induces outputs of four electrodes. When the force is released, the PDMS film will push the sphere back to initial position. The direction of shear force can be analyzed by the outputs of four electrodes. In the figure, the x-axis coincides with the angle bisector of electrode 1 and the y-axis coincides with the angle bisector of electrode 4.

For the cursor application, assuming the angle α has negligible change in each force applying cycle, therefore, the shear force has a proportional relationship with normal force. In this way, it is reasonable to represent the actual shear force output voltage amplitude by

$$V_{\text{shear}} = \sqrt{V_{\text{E1}}^2 + V_{\text{E4}}^2} \tag{2}$$

The horizontal angle θ, between the x-axis positive direction and the shear force, is derived by

$$\theta = \tan^{-1}\frac{V_{\text{E4}}}{V_{\text{E1}}} \tag{3}$$

If the amplitude of shear force and angle α are constant during the tests, the theoretical output voltage of electrode E1 is

$$V_{\text{E1}} = \frac{V_{\text{shear}}}{\sqrt{1+\tan\theta^2}} \tag{4}$$

Based on Equation (4), the theoretical output voltage values of four electrodes as shear force direction varies are shown in Table S2 (Supporting Information).

Through the theoretical derivation and force detecting mechanisms, a self-powered cursor is fabricated with 3D printing technology to characterize the applied force information, as shown in Figure 1h. The detailed fabrication process and structures are shown in Figure S3 (Supporting Information).

3. Results and Discussions

3.1. Characterization of Normal Force Detection

First, the hammer of the force gauge is set to be in exact contact with the vertex of sphere without yielding any deformation. Initially, there is no net charge generated between the two contacting surfaces of self-powered cursor. Because the sphere radius is 5 mm, the force gauge is set to run up and down 100 cycles with a displacement of 5 mm to make sure that the bottom PTFE layer is sufficiently charged. The testing setup is shown in **Figure 2**a. The application of normal force on the device is shown in Video S1 (Supporting Information).

In Figure 2b–g, 1 represents PDMS–aluminum device, 2 represents gold–PTFE device, and 3 represents galinstan–PTFE device. Figure 2b–d shows the output waveforms of open-circuit voltage, charge output, and short-circuit current under the same normal force 24.7 N. In Figure 2b, the open-circuit voltage between the bottom aluminum electrode and the ground is zero when no normal force is applied. Because the surfaces of galinstan and gold generate positive charge and PDMS surface generates negative charge, the galinstan–PTFE device and the gold–PTFE device have positive open-circuit voltage and the PDMS–aluminum device has negative open-circuit voltage. This matches well with the proposed theoretical model. Figure 2c shows the output charge of induced electrons flowing from the aluminum electrode to the ground. The initial output charge is zero when no normal force is applied. Because the bottom electrodes of galinstan–PTFE device and gold–PTFE device attract electrons and the bottom electrode of PDMS–aluminum device repels electrons, the galinstan–PTFE device and the gold–PTFE device have negative output charge and the PDMS–aluminum device has positive output charge when the normal force is applied. The results further consolidate the working mechanism model. Figure 2d shows the short-circuit current flowing from the aluminum electrode to the ground. The initial short-circuit current is zero when the applied normal force is static. As the bottom electrodes of galinstan–PTFE device and gold-PTFE device repels positive charge and the bottom electrode of PDMS–aluminum device attracts positive charge, the galinstan–PTFE device and the gold–PTFE device have positive short-circuit current peak and the PDMS–aluminum device has negative short-circuit current peak during dynamic period of normal force enhancing. In the dynamic period of normal force releasing, the galinstan–PTFE device and the gold–PTFE device have negative short-circuit current peak and the PDMS–aluminum device has positive short-circuit current peak. The result also supports the working mechanism model.

By comparing the output curves, it is easy to find out that the galinstan–PTFE configuration has the best output performance in open-circuit voltage (maximum 3.23 V), charge output (maximum 1.19 nC) and short-circuit current (peak–peak maximum 4.31 nA). The maximum voltage output of gold–PTFE device and PDMS–aluminum device are only 2.57 and 0.53 V. Based on the measured charge output amount, the surface charge density generated by galinstan–PTFE contacting is calculated to be 20.2 μC m^{-2}. Although the experimental values have some deviation from the theoretical value 168 μC m^{-2}, they are

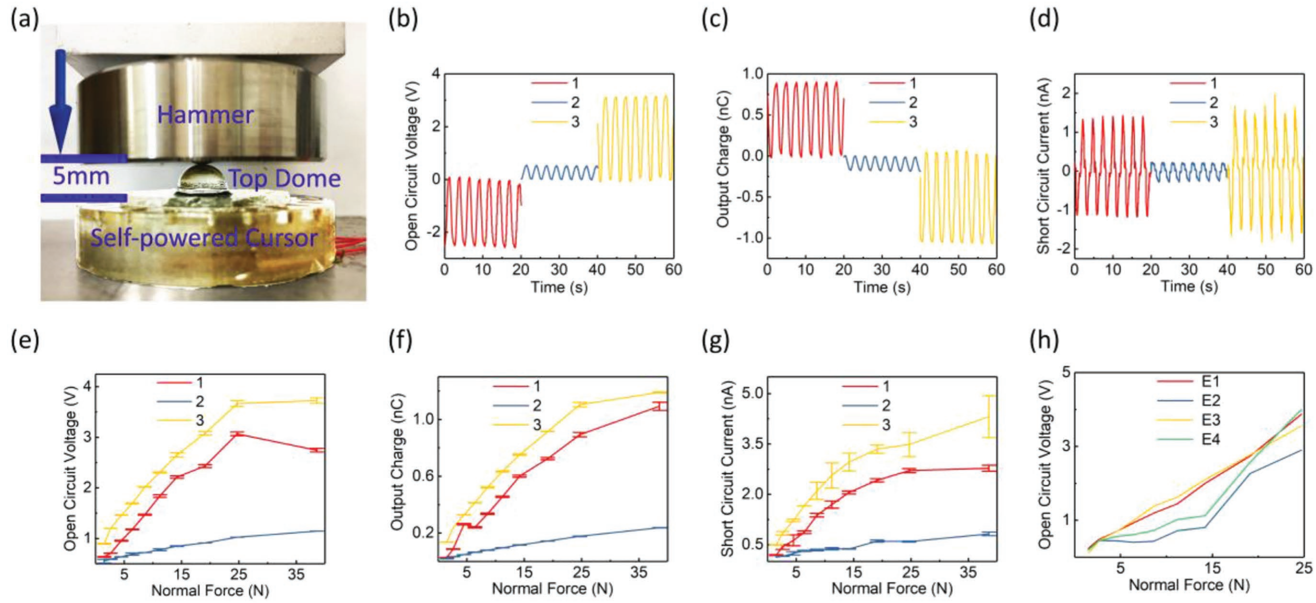

Figure 2. a) Testing setup of normal force detection. b) The open-circuit voltage of three different devices under 24.7 N normal force (1 – PDMS–aluminum device; 2 – gold–PTFE device; 3 – galinstan–PTFE device; each device is tested for continuous 20 s, here their results are combined to shown compactly in graphs (b), (c), and (d)). c) The output charge of these three devices. d) The short-circuit current of these three devices. e) The open-circuit voltage versus applied normal force. f) The output charge versus applied normal force. g) The short-circuit current versus applied normal force. h) The open-circuit voltage outputs of four-electrode configuration.

relatively comparable and reasonable for the testing environment weakens the output by many factors such as humidity, temperature, surface abrasion, fabrication defects, and so on. The surface charge density generated by gold–PTFE device is 4.04 μC m^{-2}, which is much smaller than galinstan–PTFE device. Referring to Equation (S3) and the parameter values in Table S1 (Supporting Information), the theoretical charge density value is 72.9 μC m^{-2}. This theoretical value is smaller than galinstan–PTFE device which corresponds to the measured charge density comparison of two devices. Concluded by Schein, when gold contacts with PTFE, it may even gain the negative charges.[29] Besides, its fragile property also weakens the output charge. During the experiment, fragments of gold were found attached onto the PTFE surface while galinstan has no residue on PTFE surface. Therefore, this proves that the liquid phase galinstan has superiority over other solid metals coated on the PDMS surface to contact with PTFE.

Figure 2e–g shows the relationship of output performance and the applied force. These outputs show good linear range from 0 to 25 N, which is consistent with the theoretical and simulation results. The open-circuit voltage, output charge, and short-circuit current sensitivity are 0.131 V N^{-1}, 0.048 nC N^{-1}, and 0.175 nA N^{-1}, respectively. This linear property is quite useful in the self-powered cursor application for normal force measuring. In the 25–40 N range, the output gradually saturates and the displacement of force gauge hammer finally reaches the maximum 5 mm. Because the hammer is very close to the bottom semisphere in the last step and the hammer is connected to the ground which is default set by the machine, the charge on the bottom semisphere is partially coupled by the hammer. Therefore, the outputs have a saturation trend in the range of 25–40 N which is corresponding to the displacement 4.5–5 mm of the hammer. For the PDMS–aluminum device, the open-circuit voltage becomes smaller as the applied normal force increases, while charge output and short-circuit current keep increasing to saturation in the last step. Here, bottom PDMS semisphere is the only dielectric material and has no capability of shielding electric field. Therefore, the induced positive charge on the bottom aluminum electrode is weakened by the ground-connected hammer. In the charge output and short-circuit current tests, the measurement circuit is connected directly to the ground. There is no impedance and the induced charge flows freely to the ground during the dynamic period of force applying. Therefore, the hammer has less influence on weakening induced charge of bottom electrode in contrast to open-circuit voltage tests. Additionally, the PDMS–aluminum device's output voltage is negative during the period of force applying for the bottom PDMS semisphere surface is negatively charged. The negative output property is not compatible for the majority of commercial circuits. Considering the output stability with metal shielding capability, high output performance, and positive output voltage of galinstan–PTFE device, this configuration is chosen for the self-powered cursor application which can be directly connected with the commercial portable circuits rather than the laboratory bulky instruments.

After measuring the single electrode configuration for the above three devices, the galinstan–PTFE structure is chosen to be further investigated, integrated with four separated electrodes. The open-circuit voltage outputs of four electrodes in the 0–24.7 N linear range are shown in Figure 2h. The four curves show similar linear property and comparable output amplitude comparing with single electrode device. The voltage output difference of the four electrodes is due to the fabrication and assembling deviations. In force measurements, these

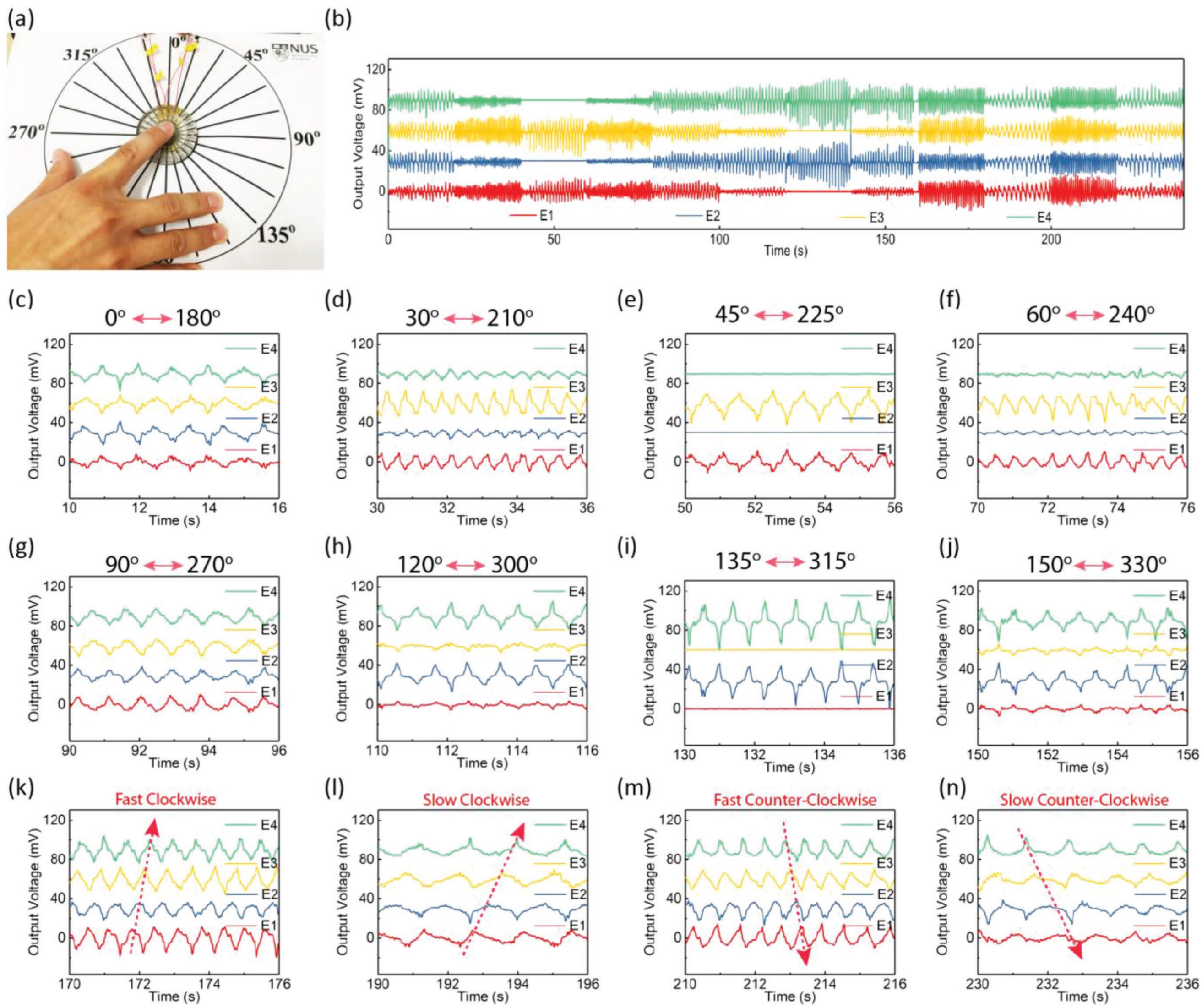

Figure 3. a) The illustration of shear force testing. b) Output voltage waveform by reciprocation and rotation motions in different directions. c–j) Zoom-in voltage waveforms of the reciprocation motions. k–n) Zoom-in voltage waveforms of the rotation motions.

discrepancies can be eliminated by normalizations which will be discussed in the next section.

3.2. Characterization of Shear Force Detection

Here, to make the testing results reliable, the force is applied at the limitation of finger capability on the top dome of the cursor keeping the same amplitude around 10 N and same vertical angle α nearly 80° in different horizontal directions. The illustration of force applied is shown in **Figure 3**a. The horizontal direction change of force is realized by following along direction scales on the sensor. The interval between two scales is 15°. Due to the low input impedance 1 MΩ of the Agilent DSO-X 3034A oscilloscope comparing to 200 TΩ of Keithley 6514 electrometer, the output voltages are only a small portion of the open-circuit voltages and have peak–peak characteristics. However, they can be used to resolve the horizontal direction of the shear force since output voltages are still proportional to the force amplitude. Additionally, the reciprocation motion of finger is repeated for more than 15 cycles to calculate the mean values of output voltage peak–peak values to elevate the accuracy and reliability of measurements.

Figure 3b includes 8 reciprocation motions and 4 rotation finger motions. Each motion contains 20 s and more than 15 voltage peaks. E1, E2, E3, and E4 are used to represent the voltage from electrode 1, electrode 2, electrode 3, and electrode 4. To differentiate the output voltage waveforms of each electrode, E2, E3, and E4 have the positive voltage offsets of 30, 60, and 90 mV, respectively. Figure 3c–j shows the zoom-in figure of each motion. Direction of 0°–180° as the reference direction (RD) represents the reciprocation motion in line with the "0°" and the "180°" scales on the sensor. The other 7 reciprocation motions have the directions of 30°, 45°, 60°, 90°, 120°, 135°, and 150°, respectively. The application of shear force is shown in Video S2 (Supporting Information). In Figure 3c, the amplitudes of E1, E2, E3, and E4 are almost the same due to the same contacting area on each electrode during the operation period. There are small differences in the magnitudes due to the fabrication deviations. Besides, E1 and E4 are in the same phase and both are in opposite phase against E2 and E3. The phase of E1 in RD is set as the reference phase. The opposite phase of the reference phase is denoted with a negative symbol "–" before the output value, as shown in Table S2 (Supporting Information). In Figure 3d, the phases of E1, E2, E3, and E4 keep the same phase as in RD. E2 and E4 are attenuated and E1 and E3 are improved because the contacting area becomes smaller for E2 and E4 but becomes larger for E1 and E3. In Figure 3e, E2 and E4 decrease to the lowest nearly zero, while E1 and E3 increase to the largest values because the contacting area are all on E1 and E3. In Figure 3f, E1 and E3 have slight attenuations and phases keep the same as in RD. E2 and E4 increase a little and phases are opposite from that in RD. In Figure 3g, E1 and E3 keep on decreasing with phases the same as in RD. E2 and E4 keep on increasing with phases opposite from RD. The amplitudes of E1, E2, E3, and E4 are almost the same as Figure 3c due to the same contacting area. In Figure 3h, E1 and E3 decrease and phases are opposite from that in RD. E2 and E4 increase with opposite phases from RD. In Figure 3i, E1 and E3 decrease to almost zero. E2 and E4 increase to the maximum. In Figure 3j, E1 and E3 increase a little, while E2 and E4 have slight attenuations. In summary, the shear force direction can be detected by the self-powered cursor through differentiating the amplitudes and phases of the four outputs.

Figure 3k–n shows the output results for the rotation motions of finger around the center of the sensor. In Figure 3k, E1, E2, E3, and E4 have a time delay in turn. This delay shows the motion is a clockwise rotation. The rotation period is 0.64 ms. In Figure 3l, E1, E2, E3, and E4 also have a time delay in turn with larger period of 1.40 ms. It is a slower clockwise rotation comparing to Figure 3k. In Figure 3m, E1, E2, E3, and E4 have a time advance in turn. This time advance shows the rotation is a counterclockwise rotation. The rotation period is 0.60 ms. In Figure 3n, E1, E2, E3, and E4 also have a time advance in turn with larger period of 1.43 ms. It is a slower counterclockwise rotation comparing with Figure 3m. The measurement of rotation motions is shown in Video S3 (Supporting Information). Therefore, except for shear force direction detection, the self-powered cursor is also able to detect the rotation direction and period of the finger motion. This greatly broadens the self-powered cursor for more advanced control applications.

Up to now, the output trends of each electrode for different force directions have been illustrated in detail. To clearly show the trends, the mean and standard deviation of E1, E2, E3, and E4 in each direction have been calculated, as shown in Table S3 (Supporting Information). To minimize the fabrication deviations, output from each electrode is normalized by the corresponding maximum value. The normalization values are shown in Table S4 (Supporting Information). The normalizations of theoretical and experimental output voltage values are compared and shown in **Figure 4**. The curves from experimental results match quite well with theoretical values from Equation (4). In Figure 4, the direction number 1, 2, 3, 4, 5, 6, 7, 8, and 9 represents the direction of 0°, 30°, 45°, 60°, 90°, 120°, 135°, 150°, and 180°, respectively. When force is applied in any horizontal direction, any two adjacent electrodes would have the positive output voltage and the other two have negative voltage, namely opposite phase. Through comparing voltage amplitude ratio and phase of the four electrode outputs, the horizontal direction of the force can be resolved accurately. With more reliable testing platform, the shear force can also be calibrated under the same vertical angle α.

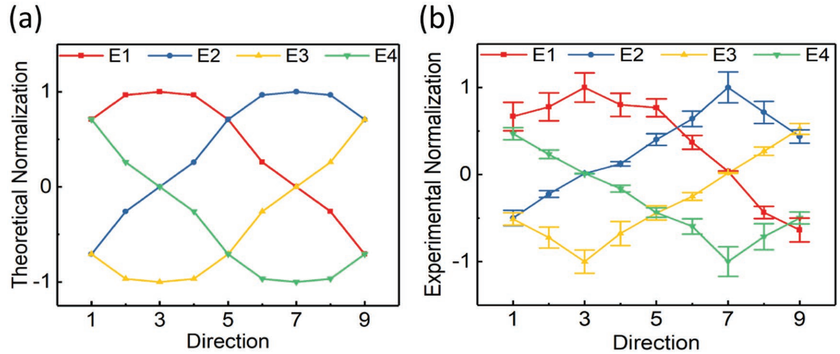

Figure 4. a) The normalization of theoretical output voltage with different shear force directions. The direction number 1, 2, 3, 4, 5, 6, 7, 8, and 9 represents the direction of 0°, 30°, 45°, 60°, 90°, 120°, 135°, 150°, and 180°, respectively. b) The normalization of experimental output voltage with different shear force directions.

To further broaden the application of the proposed self-powered cursor without the limitation of constant vertical angle α, the multiple electrodes can be deposited on the bottom electrode in the radical direction as shown in Figure S4 (Supporting Information). The shear force amplitude can be measured by the outmost electrode which lies in the boundary of contacting area and the shear force direction could be calculated in the same way as the proposed self-powered cursor. The normal force could be derived the whole output of electrodes in the contacting area. In this way, the force in any direction of half 3D space can be resolved thoroughly.

3.3. Self-Powered Cursor Demonstration

To examine whether the cursor's output voltage is compatible with present commercial portable circuits, the self-powered cursor is directly connected with Arduino Uno to control a small vehicle, as shown in **Figure 5**a. The Arduino Uno is programmed to read the output voltage of the cursor and output corresponding signals to control the small vehicle to move forward and backward. Figure 5b depicts the readout values when force is applied in 0° and 180° directions. To differentiate each electrode output in the figure, E2, E3, and E4 have a 5, 10, and 15 V positive offset against E1, respectively. The output voltage of each electrode has a voltage amplitude in the range of 0–5 V. For the force applied forward and backward cyclically, E1 and E4 are in the same phase and opposite phase against E2 and

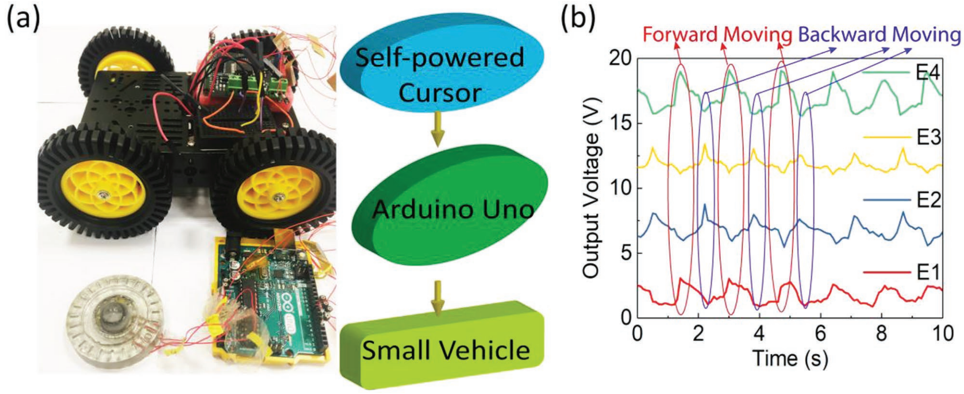

Figure 5. a) The photograph and circuit block diagram of the self-powered cursor for small vehicle control. b) The voltage output waveform read by Arduino Uno.

E3. The results match well with the theoretical and experimental output in the reciprocation motion. The demonstration of using the self-powered cursor to control the small vehicle is shown in Video S4 (Supporting Information).

4. Conclusion

A self-powered cursor is proposed and investigated with complete theoretical model, experimental characterization, and application demonstration in this work. The self-powered cursor can detect both the normal force and shear force. In detecting the normal force, it shows a linear range from 0 to 25 N. The open-circuit voltage, output charge, and short-circuit current sensitivity is 0.131 V N^{-1}, 0.048 nC N^{-1}, and 0.175 nA N^{-1}, respectively. In the aspect of shear force detection, the self-powered cursor has the capability of differentiating the horizontal direction with resolution of at least 15°. A theoretical analysis of thoroughly resolving force in any direction of half three-direction space is proposed. Additionally, this self-powered cursor is also able to detect the rotation motions circling around its touch point. Moreover, the self-powered cursor is successfully demonstrated as the interaction interface for small vehicle controlling. The self-powered cursor shows great potential for sensing and controlling in the batteryless and energy saving applications.

5. Experimental Section

Fabrication of the Self-Powered Cursor: Based on the theoretical derivation and force detecting mechanisms, a self-powered cursor was fabricated with 3D printing technology to characterize the applied force information, as shown in Figure 1h. The scales on the structure were used to denote the direction of applied force. The angle of the center point to adjacent two bars was 15°. The detailed fabrication process is shown in Figure S3a (Supporting Information). The PDMS (Sylgard 184 Dow Corning, USA) was mixed with cross-linker by the weight ratio of 10:1. The solution was then mixed with galinstan (Changsha Santech Materials, China) by the weight ratio of 1:6.44. After that, the galinstan–PDMS mixture was poured into a 3D printing mold to form the bottom semisphere. Then, pure PDMS was kept on pouring into the mold to form the supporting structure. Next, the structure was degassed and cured in the oven for 30 min under 80 °C. The structure was then demolded and packaged into another 3D printing structure with PTFE sheet and aluminum electrode on bottom. Single electrode design on the bottom of PTFE was ready for normal testing. Separated four-electrode design could be used for shear force testing. Last, PDMS touch point was bonded on top by PDMS–PDMS bonding method.[30] To compare the output performance, two other devices with the same single aluminum electrode and different structure configurations were also characterized. The three structures are shown in Figure S3b (Supporting Information).

Characterization of the Self-Powered Cursor: Open-circuit voltage, charge output measurements of the devices were conducted with electrometer (Keithley 6514). Short-circuit current was measured by Stanford SR570. The normal force applied on these devices was generated by force gauge (Mecmesin 2.5-I, Germany). The output voltage of four-electrode galinstan–PTFE device was measured by Agilent DSO-X 3034A oscilloscope. The Arduino Uno (Arduino, Italy) and small vehicle (DG012-ATV, USA) were used in the small vehicle control demonstration.

Supporting Information

Supporting Information is available from the Wiley Online Library or from the author.

Acknowledgements

This research was supported by grants from the National Research Foundation (NRF) Competitive Research Programme (CRP) project "Self-Powered Body Sensor Network for Disease Management and Prevention Oriented Healthcare" (R-263-000-A27-281), Ministry of Education (MOE) Faculty Research Committee (FRC) grant (R-263-000-B56-112) "Thermoelectric Power Generator (TEG)-Based Self-Powered ECG Plaster – System Integration (Part 3)," HiFES seed fund "Hybrid Integration of Flexible Power Source and Power Sensors," and the National Natural Science Foundation of China under grant no. 61474078 at the NUS (Suzhou) Research Institute, Suzhou, China. Additionally, assistance from Hao Wang, Tianyiyi He, and Jiahui Wang on fabrication is gratefully acknowledged. Assistance from Changhe Sun on testing is also gratefully acknowledged.

Conflict of Interest

The authors declare no conflict of interest.

Keywords

galinstan–polytetrafluoroethylene, liquid metal, self-powered cursors, tactile sensors, triboelectric nanogenerators

Received: March 7, 2018
Published online:

[1] N. Zhang, C. Tao, X. Fan, J. Chen, *J. Mater. Res.* **2017**, *32*, 1628.
[2] Z. L. Wang, J. Chen, L. Lin, *Energy Environ. Sci.* **2015**, *8*, 2250.
[3] D. Evans, *CISCO white paper*, **2011**, *1*, 1.
[4] F.-R. Fan, L. Lin, G. Zhu, W. Wu, R. Zhang, Z. L. Wang, *Nano Lett.* **2012**, *12*, 3109.
[5] L. Lin, Y. Xie, S. Wang, W. Wu, S. Niu, X. Wen, Z. L. Wang, *ACS Nano* **2013**, *7*, 8266.
[6] Y. S. Zhou, G. Zhu, S. Niu, Y. Liu, P. Bai, Q. Jing, Z. L. Wang, *Adv. Mater.* **2014**, *26*, 1719.
[7] Q. Jing, G. Zhu, W. Wu, P. Bai, Y. Xie, R. P. Han, Z. L. Wang, *Nano Energy* **2014**, *10*, 305.
[8] Y. Su, G. Zhu, W. Yang, J. Yang, J. Chen, Q. Jing, Z. Wu, Y. Jiang, Z. L. Wang, *ACS Nano* **2014**, *8*, 3843.
[9] G. Zhu, W. Q. Yang, T. Zhang, Q. Jing, J. Chen, Y. S. Zhou, P. Bai, Z. L. Wang, *Nano Lett.* **2014**, *14*, 3208.
[10] Q. Shi, H. Wu, H. Wang, H. Wu, C. Lee, *Adv. Energy Mater.* **2017**, *7*, 1701300.
[11] Q. Shi, H. Wang, H. Wu, C. Lee, *Nano Energy* **2017**, *40*, 203.
[12] Y. Yang, Y. S. Zhou, H. Zhang, Y. Liu, S. Lee, Z. L. Wang, *Adv. Mater.* **2013**, *25*, 6594.
[13] K. Parida, V. Bhavanasi, V. Kumar, R. Bendi, P. S. Lee, *Nano Res.* **2017**, *10*, 3557.
[14] Q. Shi, H. Wang, T. Wang, C. Lee, *Nano Energy* **2016**, *30*, 450.
[15] B. Meng, W. Tang, Z.-h. Too, X. Zhang, M. Han, W. Liu, H. Zhang, *Energy Environ. Sci.* **2013**, *6*, 3235.
[16] A. Chandrasekhar, N. R. Alluri, V. Vivekananthan, J. H. Park, S.-J. Kim, *ACS Sustainable Chem. Eng.* **2017**, *5*, 7310.
[17] X. He, Y. Zi, H. Yu, S. L. Zhang, J. Wang, W. Ding, H. Zou, W. Zhang, C. Lu, Z. L. Wang, *Nano Energy* **2017**, *39*, 328.
[18] Z. Wang, R. Jiang, G. Li, Y. Chen, Z. Tang, Y. Wang, Z. Liu, H. Jiang, C. Zhi, *ACS Appl. Mater. Interfaces* **2017**, *9*, 22685.
[19] X. Zhang, Y. Zheng, D. Wang, F. Zhou, *Nano Energy* **2017**, *40*, 95.
[20] Z. L. Wang, *Faraday Discuss.* **2015**, *176*, 447.
[21] G. Zhu, C. Pan, W. Guo, C.-Y. Chen, Y. Zhou, R. Yu, Z. L. Wang, *Nano Lett.* **2012**, *12*, 4960.
[22] S. Wang, L. Lin, Z. L. Wang, *Nano Lett.* **2012**, *12*, 6339.
[23] R. D. I. G. Dharmasena, K. Jayawardena, C. Mills, J. Deane, J. Anguita, R. Dorey, S. Silva, *Energy Environ. Sci.* **2017**, *10*, 1801.
[24] Z. L. Wang, *Mater. Today* **2017**, *20*, 74.
[25] A. Fassler, C. Majidi, *Adv. Mater.* **2015**, *27*, 1928.
[26] A. Wåhlin, G. Bäckström, *J. Appl. Phys.* **1974**, *45*, 2058.
[27] D. Davies, *J. Phys. D: Appl. Phys.* **1969**, *2*, 1533.
[28] J. Wang, C. Wu, Y. Dai, Z. Zhao, A. Wang, T. Zhang, Z. L. Wang, *Nat. Commun.* **2017**, *8*, 88.
[29] L. B. Schein, *Electrophotography and Development Physics*, Vol. *14*, Springer Science & Business Media, Berlin **2013**.
[30] M. A. Eddings, M. A. Johnson, B. K. Gale, *J. Micromech. Microeng.* **2008**, *18*, 067001.